

# Highly Efficient Air-Mode Silicon Metasurfaces for Visible Light Operation Embedded in a Protective Silica Layer

Qian Sun, Haowen Liang,\* Jianchao Zhang, Weibin Feng, Emiliano R. Martins, Thomas F. Krauss, and Juntao Li\*

Dielectric metasurfaces have significant potential for delivering miniaturized optical systems with versatile functionalities, leading to applications in various fields such as orbital angular momentum generation, imaging, and holography. Among the different materials, crystalline silicon has the advantage of technological maturity and high refractive index, which increases design flexibility and processing latitude. The second, and often overlooked, advantage of silicon is that it affords embedding the metasurface in a protective material such as silica, which is essential for practical applications. The trade-off against this high refractive index is silicon's absorption at visible wavelength, which requires new design strategies. Here, such a strategy based on metasurfaces supporting air modes is identified that can lead to a transmission efficiency as high as 87% at a wavelength of 532 nm. This exceptional efficiency is obtained by using the high index to confine the electric field in the periphery of the meta-atoms, thereby reducing absorption losses. As an example, the design of a fully embedded metasurface is described that can generate vortex beams with various orders of orbital angular momentum. It is envisioned that the proposed strategy paves the way for practical applications of high-efficiency metasurfaces based on crystalline silicon.

## 1. Introduction

Metasurfaces are composed of meta-atoms, which are nanostructures that impose a local modulation on an incoming wavefront to achieve a desired optical functionality,<sup>[1–3]</sup> such as orbital angular momentum (OAM) generation,<sup>[4–9]</sup> metalenses,<sup>[10–18]</sup> and holograms.<sup>[19–25]</sup> Their small footprint, subwavelength thickness and compatibility with large-scale fabrication techniques have provided a new research direction in nanophotonics and have excited the community about the opportunities offered by “flat optics” as one of the top 10 emerging technologies in 2019.<sup>[26]</sup>

Recent research has focused on realizing metasurfaces in dielectric materials following the recognition that earlier plasmonic realizations were too lossy, especially when operated in transmission.<sup>[1,2,27]</sup> Indeed, high efficiencies around 90% at 532 nm<sup>[15]</sup> have been obtained with dielectric metasurfaces made of materials

of moderate refractive index  $n$  and very low extinction coefficient  $k$ , such as  $\text{TiO}_2$  and  $\text{GaN}$ .<sup>[28]</sup> For many applications, however, it is necessary to embed the metasurface in a background material with a planarized surface, e.g., to provide a protective coating,<sup>[29]</sup> to increase the numerical aperture using a high-index oil<sup>[11]</sup> or to realize multilayer structures.<sup>[10,30]</sup> In these scenarios, and to generate the phase delay required for efficient modulation, it is of great advantage to build the metasurface with dielectric materials of high refractive index.


Crystalline silicon (c-Si) appears as a natural choice,<sup>[11,13,36,22–24,31–35]</sup> as it is a high index material that is available at high quality and compatible with CMOS processes, which is important for scale-up manufacturing. Different optimization methods have already been used to reduce the impact of silicon absorption on metasurface performance.<sup>[11,34,35]</sup> Hence, despite its well-known absorption in the visible regime (e.g.,  $\alpha \approx 10^4 \text{ cm}^{-1}$  at 532 nm), we have already shown high focusing efficiency (67% in transmission) and high NA (NA = 1.47) operation at this wavelength,<sup>[11]</sup> the latter having been achieved via high-index oil immersion. Furthermore, c-Si metasurfaces with more than 60% transmission efficiency have also been demonstrated in deflection,<sup>[31,35]</sup> for OAM generation,<sup>[32]</sup> and for holography applications.<sup>[23,24]</sup> The high index of

Q. Sun, Prof. H. Liang, J. Zhang, W. Feng, Prof. J. Li  
State Key Laboratory of Optoelectronic Materials and Technologies  
School of Physics  
Sun Yat-Sen University  
Guangzhou 510275, China  
E-mail: lianghw26@mail.sysu.edu.cn; lij3@mail.sysu.edu.cn

Prof. H. Liang  
Southern Marine Science and Engineering Guangdong Laboratory  
(Zhuhai)  
Zhuhai 519080, China

Prof. E. R. Martins  
São Carlos School of Engineering  
Department of Electrical and Computer Engineering  
University of São Paulo  
São Carlos, SP 13566-590, Brazil

Prof. T. F. Krauss  
Department of Physics  
University of York  
York YO10 5DD, UK

 The ORCID identification number(s) for the author(s) of this article can be found under <https://doi.org/10.1002/adom.202002209>.

DOI: 10.1002/adom.202002209

silicon has also enabled the first demonstration of a metalens with a field of view as high as  $\pm 89^\circ$ .<sup>[36]</sup> The question is whether this performance can be improved even further and made comparable with that achieved in  $\text{TiO}_2$ , which has demonstrated multiple functionalities and an efficiency up to  $\eta \approx 90\%$ . In order to answer this question, we have identified a metasurface design strategy that is more tolerant to absorption losses, thus paving the way to the highest efficiency operation also in crystalline silicon.

Our design uses meta-atoms composed of c-Si nanobricks, similar to those used by Khorasaninejad et al.,<sup>[12]</sup> but we extend the design to utilize air modes that are mainly situated in the space between the nanobricks yet with their electric field at the periphery of the nanobricks, which helps to mitigate the absorption losses.

To exemplify this strategy, we have chosen the important problem of high order OAM generation, which has a number of applications, such as high-purity OAM laser,<sup>[4]</sup> high capacity optical communication,<sup>[37,38]</sup> and multiplexing channels OAM holography.<sup>[25,39]</sup> We realize OAM beams using the Pancharatnam–Berry (PB) phase approach; we design the metasurface to be embedded in silica, to operate at a wavelength of 532 nm and predict a transmission as high as 87%.

## 2. Theory and Methods

The structure is illustrated in **Figure 1**. The PB phase modulation is achieved by rotating the meta-atoms that act as miniature half-waveplates. A straightforward Jones matrix analysis shows that, when circularly polarized light is incident on a wave-plate with a rotation angle of  $\theta$ , then a phase shift  $\Phi = \pm 2\theta$  is imposed on the orthogonal circular polarization state, where “+” is applied for left-circularly polarized incident light while “−” is applied for right-circularly polarized light.<sup>[40]</sup> Therefore, it is possible to control the transmission phase  $\Phi$  by tuning the geometrical phase  $\theta$ . See Section S1 (Supporting Information) for more details on the Jones matrix description of the PB phase.

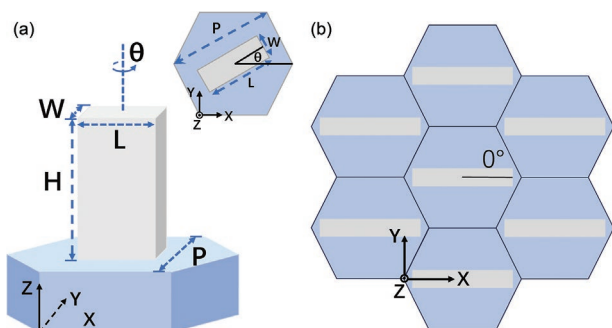


**Figure 1.** a) Schematic of the nanobrick in a hexagonal unit cell. The inset is the top view of a single unit cell.  $W$ ,  $L$ ,  $H$  are the width, length, and height of the nanobrick, respectively;  $P$  is the distance between the two parallel sides of the hexagonal lattice;  $\theta$  represents the rotation angle between the major axis of the nanobrick and the  $X$  direction. b) Top view of the layout of nanobricks during the optimization procedure when the rotation angle is 0. The gray rectangle represents the c-Si nanobrick.

There are four parameters of the c-Si nanobrick to be determined: length ( $L$ ), width ( $W$ ), height ( $H$ ) and the period of the unit cell ( $P$ ) as illustrated in Figure 1a. The layout of the nanobricks during the optimization procedure is depicted in Figure 1b, where the rotation angle of the nanobrick  $\theta$  is 0. Periodic boundary conditions are applied in  $X$  and  $Y$  direction. A hybrid optimization algorithm (HOA)<sup>[11]</sup> is then used to find the optimized parameters of the c-Si nanobrick for 532 nm wavelength operation. We note that, to optimize the efficiency of the PB phase modulation, the array has to impose a  $\pi$  phase shift while maintaining a high and uniform transmission along the two principal axes of polarization.<sup>[40,41]</sup> The PB phase is utilized here due to its characteristic of equal size of all nanobricks, which supports the air-mode irrespective of phase. It should also be noted that several sets of optimized parameters are obtained with the help of HOA, but the design described hereafter is chosen due to its larger period, which facilitates the fabrication.

The design achieves a maximum conversion efficiency of 88% at  $15^\circ$ ,  $75^\circ$ , and  $135^\circ$ , as shown by the red curve of **Figure 2a**. The conversion efficiency is defined as the ratio of the converted circularly polarized light (right-circularly polarized light) to the incident light (left-circularly polarized light). This high conversion efficiency, even in the presence of absorption losses, arises because of the air-mode design<sup>[42,43]</sup> resulting in a concentration of the electric field in the space between the nanobricks. The electric field profiles are shown in Figure 2b, where the field confinement out of the c-Si nanobricks can

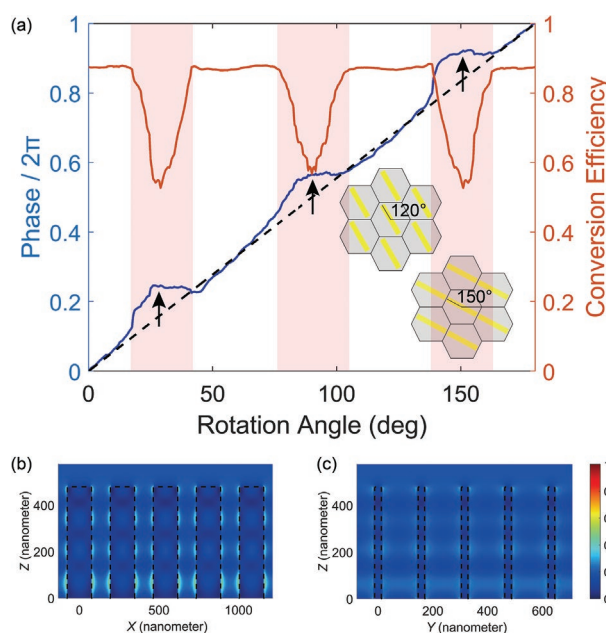


**Figure 2.** a) Simulated conversion efficiency (red line) and phase (blue line) of the optimized c-Si nanobrick. The black dashed line represents the ideal phase control which is twice the rotation angle when illuminated with left-circularly polarized light. Electric field profile for the case of  $\theta = 0$  (Figure 1b) in b) the  $X$ - $Z$  plane and c) the  $Y$ - $Z$  plane. The dashed black lines depict the boundaries of the nanobricks. The parameters of the optimized c-Si nanobricks are as follows:  $L = 151$  nm,  $W = 26$  nm,  $H = 476$  nm,  $P = 153$  nm. The background refractive index is 1.5. The arrows highlight the angles of  $30^\circ$ ,  $90^\circ$ , and  $150^\circ$ .

clearly be seen, which minimizes overlap with the lossy material and therefore absorption losses of the metasurface device. In order to quantify the electric field confined inside ( $E_{in}$ ) and outside ( $E_{out}$ ) of the nanobricks, we determine the absolute value of the electric field in the two regions and find that the ratio of  $E_{out}/E_{in}$  is 7.36, in accordance with Figure 2b.

The ideal PB phase is shown as the dashed black line in Figure 2a. It is clear that there is some coupling effect, which induces a phase deviation for the angles where the meta-atoms are close to touching, but otherwise, the PB phase (blue line) closely follows the ideal phase. The phase deviation follows the  $60^\circ$  rotational symmetry of the hexagonal lattice and occurs for rotation angles around  $30^\circ$ ,  $90^\circ$ , and  $150^\circ$ , as highlighted by the red stripes of Figure 2a. The phase deviation is clearly accompanied by a drop in conversion efficiency. As illustrated in Figure 2a, the nanobricks are aligned at these angles, resulting in a vanishingly small gap. Figure S1 (Supporting Information) shows the corresponding electric field profiles which highlight the strong coupling effect between the nanobricks upon alignment. This strong coupling effect results in the conversion efficiency dip and phase mismatch (for detail, see Section S1, Supporting Information). As discussed below, in order to maintain high efficiency, we will therefore avoid these rotation angles in our design; avoiding these angles is also advantageous technologically, as it would be very challenging to fabricate such small features reproducibly.

The advantage of using the air-mode can be appreciated by comparing our design to one that does not support air modes (for detail, see Section S2, Supporting Information) and which has a maximum conversion efficiency of 77%. In the absence of the air-mode, the electric field is confined more strongly to the nanobricks, thus increasing absorption and limiting the conversion efficiency. A further comparison is made with an array made of  $\text{TiO}_2$  with its parameters taken from reference.<sup>[44]</sup> The  $\text{TiO}_2$  array is nonabsorbing, thus allowing a high conversion efficiency. Based on the data,<sup>[44]</sup> our simulation shows that a maximum simulation conversion efficiency of 92% can be achieved (Figure S3, Supporting Information). By immersing the  $\text{TiO}_2$  lens in water or oil, however, the efficiency drops significantly<sup>[28,45]</sup> (by a factor 1.5–2), which does not occur for the silicon-based lens.

In order to optimize the efficiency of the metasurface, we refer to the phase map (Figure 2) and simply omit the regions highlighted by the red stripes. In these cases, the rotation angle with the maximum conversion efficiency is selected. Furthermore, for

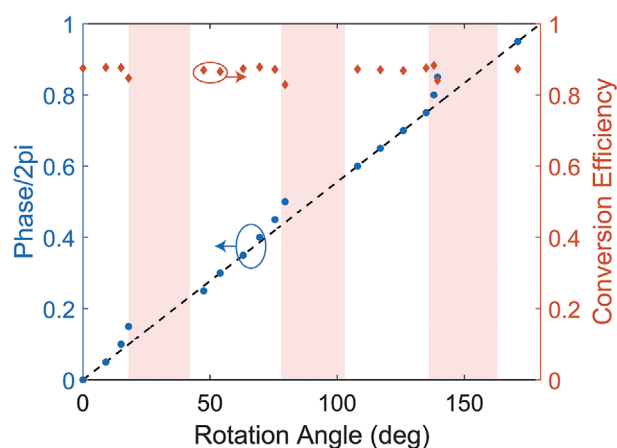


**Figure 3.** Phase (blue dots) and conversion efficiency (red diamonds) map for the optimized c-Si nanobrick design. The black dashed line depicts the ideal PB phase. Phase compensation can be achieved by choosing the rotation angles according to the phase map, instead of using the linear relation represented by the black dashed line. The low conversion efficiency regions are highlighted by the red stripes. Notice that most points actually used for the design lie outside these regions of low efficiency.

any metasurface design, the full  $2\pi$  phase is typically discretized, e.g., in  $\pi/8$  or  $\pi/10$  increments, so we can choose a discretization which avoids the critical sections. Figure 3 shows a possible realization whereby the red diamonds represent the data points actually used in our design. The black dashed line depicts the ideal PB phase as in Figure 2. Notice that most of the red diamonds lie outside the “red stripe” low conversion efficiency regions. This phase conversion efficiency map with 17 efficient points can now be used to design metasurfaces with specific functionalities, e.g., high order OAM generation; examples are shown in Section 3.

### 3. OAM Generator Metasurfaces

The advantage of our air-mode design is finally exemplified via an OAM generator where we use the c-Si nanobrick geometry to generate OAM beams of different orders and with high transmission efficiency.

The simulated intensity distributions for orders 1, 5, and 10 are shown in Figure 4; other orders and corresponding

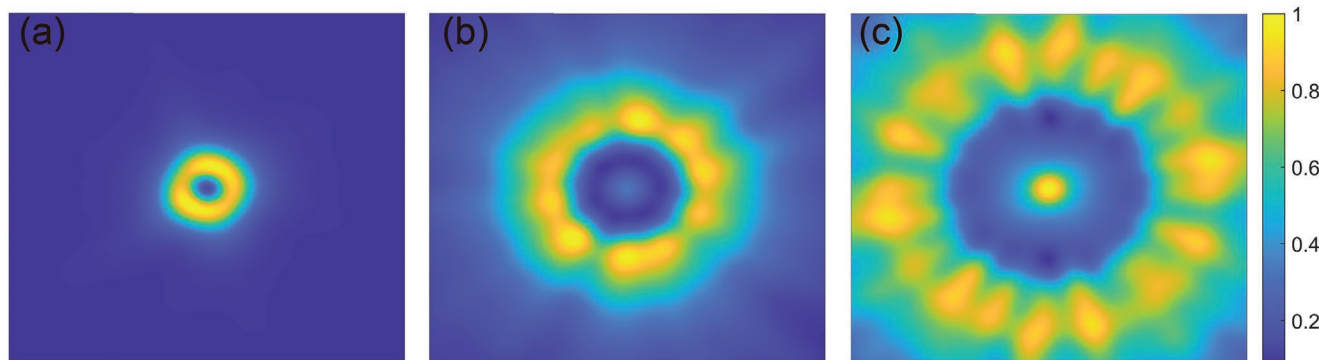


**Figure 4.** Simulated light intensity distribution of OAM generator metasurfaces with different orders of a)  $l = 1$ , b)  $l = 5$ , and c)  $l = 10$ . The corresponding transmission efficiencies are a) 87%, b) 85%, and c) 83%.

converted light intensity distributions are shown in Section 3 (Supporting Information). The c-Si nanobricks utilized here are the same as those shown in Figure 2:  $L = 151$  nm,  $W = 26$  nm,  $H = 476$  nm,  $P = 153$  nm. The desired phase profiles of the different orders  $l$  of OAM beams can be expressed as  $\exp(il\varphi)$ , where  $\varphi$  is the azimuthal angle. This phase profile is then discretized into hexagonal lattices according to the phase map of 17 points shown in Figure 3. As an example, for the canonical vortex beam of topological charge 1, the characteristic “donut” shape is clearly observed (Figure 4a). Importantly, the simulated transmission of these embedded metasurfaces reaches a remarkable value of 87% for topological charge  $l = 1$ . For higher orders, the efficiency drops slightly (to 85% for  $l = 5$  and 83% for  $l = 10$ ). The transmission efficiency is defined as the ratio of the transmitted light passing through the OAM generator to the incident light. We also note slight imperfections in the beam shape, which is the small penalty for missing some amplitude terms<sup>[4,46]</sup> (see also Section 4, Supporting Information).

We emphasize that the above demonstration of an OAM generator is only one of many possible examples, and that other highly performing metasurface functionalities can be achieved using the air-mode design introduced here.

## 4. Discussion and Conclusion

We have introduced a new design for creating metasurfaces utilizing the PB phase; the PB phase uses the geometrical rotation of meta-atoms shaped as “nanobricks” to impart a phase change onto a circularly polarized input beam. Our design exploits the phenomenon of air modes that can be confined between high refractive index nanostructures; by using these air modes and confining the optical field near the edge of the nanobricks, it is possible to maintain the phase control required for metasurface operation while minimizing the impact of the strong absorption of silicon. As a result, we are able to predict a conversion efficiency as high as 87% at a wavelength of 532 nm, which is very close to the value of 90% achieved with a  $\text{TiO}_2$  array.

In addition, we explore the important issue of embedding the metasurface in a protective medium, such as silica or a polymer. The issue of embedding is rarely considered in the literature and results are typically only shown for “bare” metasurfaces whereby the nanostructure is directly exposed to air. In contrast, for real-world applications, it is generally accepted that it is preferable to embed such fragile nanostructures in a protective medium. Embedding the silicon metasurface has little impact on its optical functionality given the high refractive index of the material, i.e., the 87% quoted above were actually achieved for a fully embedded structure. In contrast, the lower index of  $\text{TiO}_2$  and  $\text{Si}_3\text{N}_4$  make these materials much more susceptible to local refractive index changes with a reported efficiency loss of a factor 1.5–2.

These observations combine to lead us to the remarkable conclusion that high refractive index is more important than loss for a metasurface material, which is quite a profound insight.

The downside of the approach we put forward here is two-fold, namely a) very small period and feature size, and b) coupling between the nanobricks for certain rotation angles, in

particular when the bricks almost touch. These issues can be addressed as follows:

- The smaller period of  $P = 153$  nm we propose is a direct consequence of the embedded design and the increase in effective index it produces. Reducing the period is therefore a challenge facing most metasurface designs as they aim to enter the realm of practical applications. The technological difficulty of defining and reproducing meta-atoms is made somewhat easier, however, when the meta-atoms are of equal size, as is the case for the PB approach; the fill-factor of a PB metasurface does not change irrespective of the desired phase, which mitigates proximity effects that occur during lithography. We note that we have already produced a metasurface with a different, polarization-independent design whereby the size of the meta-atoms does change as a function of the desired phase. This design is more difficult to produce, yet we have experimentally demonstrated high-performance operation with a period of 190 nm.<sup>[36]</sup> We therefore believe that a PB phase metasurface of 153 nm period is realistically achievable. In terms of feature size, we also note that a similar aspect ratio of 40 nm width and 600 nm height has already been successfully demonstrated with silicon nanobricks<sup>[22]</sup> further supporting the feasibility of our design. Note that we also discuss design tolerances in Section 5 (Supporting Information).
- Regarding the coupling problem, we already propose a solution, which is to avoid the most critical geometries, as highlighted by the red stripes in Figure 3. We show that even by omitting certain points from the phase map, demanding functions, such as higher order OAM beam generation can be successfully realized.

In conclusion, the air-mode design we propose here provides a realistic route to producing high-efficiency silicon metasurfaces with all the technological advantages offered by the silicon industry; moreover, the design embeds the meta-atoms in a protective dielectric coating which makes it most suitable for practical applications. Our work therefore supports the claim of using silicon as the material of choice for high-performance metasurface realizations.

## 5. Experimental Section

There are four parameters of the c-Si nanobrick to be determined:  $L$ ,  $W$ ,  $H$  and  $P$  of the unit cell. A self-adaptive HOA was used to search the global optimized set of parameters with the objective to achieve a  $\pi$  phase delay while attaining high and uniform transmission. For more details of the optimization procedure, see ref. [11]. The phase control and conversion efficiency of the nanobrick array were then calculated using the commercial software FDTD Solutions (Lumerical Inc.) based on the finite difference time domain (FDTD) method. In the FDTD simulation, left-circularly polarized light of 532 nm wavelength was injected from the substrate. The boundary conditions were periodic along the  $X$  and  $Y$  direction and perfectly matched layers (PMLs) along the  $Z$  direction was used. The simulation of the OAM generator metasurfaces was also carried out in FDTD, applying PML boundary conditions in all directions with 532 nm left-circularly polarized light injected from the substrate direction.

## Supporting Information

Supporting Information is available from the Wiley Online Library or from the author.

## Acknowledgements

This work was supported by the Guangdong Provincial Key R&D Program (No. 2019B010152001), National Natural Science Foundation of China (Nos. 11974436, 12074444, and 11704421), Guangdong Basic and Applied Basic Research Foundation (Nos. 2020B1515020019 and 2020A151501184). H.L. acknowledges support by Innovation Group Project of Southern Marine Science and Engineering Guangdong. E.R.M. acknowledges support by Grant No. 2020/00619-4, São Paulo Research Foundation (FAPESP). T.F.K. acknowledges support by UK Research & Innovation under Contract Nos. EP/P030017/1 and EP/T020008/1.

## Conflict of Interest

The authors declare no conflict of interest.

## Data Availability Statement

The data that supports the findings of this study are available in the supplementary material of this article.

## Keywords

crystalline silicon, optical metasurfaces, visible wavelength

Revised: March 9, 2021  
Published online: April 21, 2021

- [1] P. Genevet, F. Capasso, F. Aieta, M. Khorasaninejad, R. Devlin, *Optica* **2017**, 4, 139.
- [2] H.-T. Chen, A. J. Taylor, N. Yu, *Rep. Prog. Phys.* **2016**, 79, 076401.
- [3] D. Neshev, I. Aharonovich, *Light Sci. Appl.* **2018**, 7, 58.
- [4] H. Sroor, Y.-W. Huang, B. Sephton, D. Naidoo, A. Vallés, V. Ginis, C.-W. Qiu, A. Ambrosio, F. Capasso, A. Forbes, *Nat. Photonics* **2020**, 14, 498.
- [5] L. Huang, X. Song, B. Reineke, T. Li, X. Li, J. Liu, S. Zhang, Y. Wang, T. Zentgraf, *ACS Photonics* **2017**, 4, 338.
- [6] R. C. Devlin, A. Ambrosio, D. Wintz, S. L. Oscurato, A. Y. Zhu, M. Khorasaninejad, J. Oh, P. Maddalena, F. Capasso, *Opt. Express* **2017**, 25, 377.
- [7] R. C. Devlin, A. Ambrosio, N. A. Rubin, J. P. B. Mueller, F. Capasso, *Science* **2017**, 358, 896.
- [8] F. Bouchard, I. De Leon, S. A. Schulz, J. Upham, E. Karimi, R. W. Boyd, *Appl. Phys. Lett.* **2014**, 105, 101905.
- [9] S. Chen, Y. Cai, G. Li, S. Zhang, K. W. Cheah, *Laser Photonics Rev.* **2016**, 10, 322.
- [10] Y. Zhou, I. I. Kravchenko, H. Wang, J. R. Nolen, G. Gu, J. Valentine, *Nano Lett.* **2018**, 18, 7529.
- [11] H. Liang, Q. Lin, X. Xie, Q. Sun, Y. Wang, L. Zhou, L. Liu, X. Yu, J. Zhou, T. F. Krauss, J. Li, *Nano Lett.* **2018**, 18, 4460.
- [12] M. Khorasaninejad, W. T. Chen, R. C. Devlin, J. Oh, A. Y. Zhu, F. Capasso, *Science* **2016**, 352, 1190.
- [13] J. Chen, F. Zhang, Q. Li, J. Wu, L. Wu, *Opt. Express* **2018**, 26, 34919.
- [14] J.-S. Park, S. Zhang, A. She, W. T. Chen, P. Lin, K. M. A. Yousef, J.-X. Cheng, F. Capasso, *Nano Lett.* **2019**, 19, 8673.
- [15] B. H. Chen, P. C. Wu, V.-C. Su, Y.-C. Lai, C. H. Chu, I. C. Lee, J.-W. Chen, Y. H. Chen, Y.-C. Lan, C.-H. Kuan, D. P. Tsai, *Nano Lett.* **2017**, 17, 6345.
- [16] W. T. Chen, A. Y. Zhu, V. Sanjeev, M. Khorasaninejad, Z. Shi, E. Lee, F. Capasso, *Nat. Nanotechnol.* **2018**, 13, 220.
- [17] A. Arbabi, Y. Horie, A. J. Ball, M. Bagheri, A. Faraon, *Nat. Commun.* **2015**, 6, 7069.
- [18] H. Chen, Z. Wu, Z. Li, Z. Luo, X. Jiang, Z. Wen, L. Zhu, X. Zhou, H. Li, Z. Shang, Z. Zhang, K. Zhang, G. Liang, S. Jiang, L. Du, G. Chen, *Opt. Express* **2018**, 26, 29817.
- [19] X. Ni, A. V. Kildishev, V. M. Shalae, *Nat. Commun.* **2013**, 4, 2807.
- [20] W. Zhao, H. Jiang, B. Liu, J. Song, Y. Jiang, C. Tang, J. Li, *Sci. Rep.* **2016**, 6, 30613.
- [21] H. Zhou, B. Sain, Y. Wang, C. Schlickriede, R. Zhao, X. Zhang, Q. Wei, X. Li, L. Huang, T. Zentgraf, *ACS Nano* **2020**, 14, 5553.
- [22] Y. Bao, Y. Yu, H. Xu, C. Guo, J. Li, S. Sun, Z.-K. Zhou, C.-W. Qiu, X.-H. Wang, *Light Sci. Appl.* **2019**, 8, 95.
- [23] A. Martins, J. Li, A. F. da Mota, V. M. Pepino, Y. Wang, L. G. Neto, F. L. Teixeira, E. R. Martins, B.-H. V. Borges, *Opt. Express* **2018**, 26, 30740.
- [24] A. Martins, J. Li, A. F. da Mota, Y. Wang, L. G. Neto, J. P. do Carmo, F. L. Teixeira, E. R. Martins, B.-H. V. Borges, *Opt. Express* **2018**, 26, 9573.
- [25] H. Ren, X. Fang, J. Jang, J. Bürger, J. Rho, S. A. Maier, *Nat. Nanotechnol.* **2020**, 15, 948.
- [26] B. Brouwers, Top 10 Emerging Technologies (3): Tiny Lenses – Innovation Origins, <https://innovationorigins.com/top-10-emerging-technologies-3-tiny-lenses/> (accessed: December 2020).
- [27] P. R. West, S. Ishii, G. V. Naik, N. K. Emani, V. M. Shalae, A. Boltasseva, *Laser Photonics Rev.* **2010**, 4, 795.
- [28] W. T. Chen, A. Y. Zhu, F. Capasso, *Nat. Rev. Mater.* **2020**, 5, 604.
- [29] A. Arbabi, E. Arbabi, S. M. Kamali, Y. Horie, S. Han, A. Faraon, *Nat. Commun.* **2016**, 7, 13682.
- [30] A. McClung, M. Mansouree, A. Arbabi, *Light Sci. Appl.* **2020**, 9, 93.
- [31] Z. Zhou, J. Li, R. Su, B. Yao, H. Fang, K. Li, L. Zhou, J. Liu, D. Stellinga, C. P. Reardon, T. F. Krauss, X. Wang, *ACS Photonics* **2017**, 4, 544.
- [32] H. Li, D. P. Stellinga, Y. Qiu, Q. Sun, B. Chen, H. Liang, T. F. Krauss, J. Li, *Opt. Express* **2019**, 27, 30931.
- [33] Y. Qiu, F. Zhao, X. Zhu, J. Li, H. Liang, J. Wang, Z. Cai, *J. Phys. D: Appl. Phys.* **2019**, 52, 084001.
- [34] J. Yang, J. A. Fan, *Opt. Express* **2017**, 25, 23899.
- [35] D. Sell, J. Yang, S. Doshay, K. Zhang, J. A. Fan, *ACS Photonics* **2016**, 3, 1919.
- [36] A. Martins, K. Li, J. Li, H. Liang, D. Conteduca, B.-H. V. Borges, T. F. Krauss, E. R. Martins, *ACS Photonics* **2020**, 7, 2073.
- [37] A. E. Willner, H. Huang, Y. Yan, Y. Ren, N. Ahmed, G. Xie, C. Bao, L. Li, Y. Cao, Z. Zhao, J. Wang, M. P. J. Lavery, M. Tur, S. Ramachandran, A. F. Molisch, N. Ashrafi, S. Ashrafi, *Adv. Opt. Photonics* **2015**, 7, 66.
- [38] S. Yu, *Opt. Express* **2015**, 23, 3075.
- [39] X. Fang, H. Ren, M. Gu, *Nat. Photonics* **2020**, 14, 102.
- [40] E. Hasman, V. Kleiner, G. Biener, A. Niv, *Appl. Phys. Lett.* **2003**, 82, 328.
- [41] M. Kang, T. Feng, H.-T. Wang, J. Li, *Opt. Express* **2012**, 20, 15882.
- [42] V. R. Almeida, Q. Xu, C. A. Barrios, M. Lipson, *Opt. Lett.* **2004**, 29, 1209.
- [43] Q. Xu, V. R. Almeida, R. R. Panepucci, M. Lipson, *Opt. Lett.* **2004**, 29, 1626.
- [44] B. Groever, W. T. Chen, F. Capasso, *Nano Lett.* **2017**, 17, 4902.
- [45] W. T. Chen, A. Y. Zhu, M. Khorasaninejad, Z. Shi, V. Sanjeev, F. Capasso, *Nano Lett.* **2017**, 17, 3188.
- [46] B. Sephton, A. Dudley, A. Forbes, *Appl. Opt.* **2016**, 55, 7830.